

Dynamics of Vacuum Decay

Dalila Maria Pîrvu

An essay submitted
for partial fulfillment of
Perimeter Scholars International

June, 2020

Contents

1	Introduction	2
2	Vacuum Decay	6
2.1	The Instanton Formalism	6
2.2	A Semiclassical Approach	10
3	The Wigner Formalism	12
4	Towards the Bubble-Bubble Correlation Function	15
4.1	The Two-Point Autocorrelation Function	16
4.2	The Peak-Peak Correlation Function	19
5	Vacuum Decay from Scattering	24
6	Conclusion	29
7	Acknowledgements	30
	References	30
A	Statistics of the Free Gaussian Random Field	33
B	Lattice Field Theory	34

Dynamics of Vacuum Decay

Dalila Maria Pîrvu

Supervisor: Matthew C. Johnson

False vacuum decay in quantum mechanical first order phase transitions is a phenomenon with wide implications in the early Universe, and presents interesting theoretical challenges. In this work, we implement a semi-classical stochastic approach to study vacuum decay that was developed in [1]. We go beyond the predictions of the standard instanton-based formalism [2, 3] and explore the dynamical evolution of the problem. Specifically, we approximate the state of time-evolving fields through Wigner functionals obtained from ensemble averages of classical lattice simulations with different initial conditions. We look at the correlation functions of a stochastic $(1 + 1)$ -dimensional classic field to investigate its statistical properties and compare them against the predictions for a quantum relativistic scalar field. The tools we are developing can be applied to the study of correlations between bubble nucleation sites for a field at the false vacuum. We also prove that the addition of quantum fluctuations to false vacuum particle scattering leads to decay in classically forbidden regions in the energy space. The present study is a first step towards building a more solid description of time dependence in vacuum decay.

Statement of original research

Chapters 1, 2 and 3 in this essay contain a literature review; Chapter 4 reproduces results in [4–6]; Chapter 5 describes original work. The results and future directions of work are summarised in Chapter 6. All data is simulated using a code developed by J. Braden [1, 7] with a few original adaptations.

1 Introduction

Relativistic first order phase transitions take place in field theories with an associated potential that has two non-degenerate vacuum states. Given a large region of flat space localised around the false minimum, the system will want to minimise its energy and occupy the true vacuum. There are several ways it can do so. It can receive an input of energy to overcome the potential barrier classically, or it can experience thermal and quantum mechanical fluctuations associated with the energy of the false vacuum state, that can trigger the decay. Eventually, and locally, a finite region will cross the potential barrier towards the true minimum. In order to compensate for the change in energy density, a boundary layer is created that is called the bubble wall. Bubbles can materialise throughout the whole available space, and as they expand and collide, undergoing all kinds of dynamics dictated by the shape of the underlying potential. The phase transition ends when the entire volume is turned into a state localised around the true vacuum.

There is strong motivation to study relativistic phase transitions in the context of quantum field theory (QFT), as an infinite dimensional counterpart for quantum mechanical tunnelling. This phenomenon is a non-perturbative, non-equilibrium, non-linear problem, a regime where we don't have a good theoretical description and our usual perturbative methods break down. Yet, it relates to fundamental issues in quantum theory such as the emergence of classicality and decoherence, because the bubble is a macroscopical, classical object, which can form as a consequence to the stochastic interactions of a quantum system.

Applied to curved spacetimes, false vacuum decay has numerous applications in modern cosmology. The most prevalent application is in models of inflation. Inflation is a period of exponential expansion of the early Universe, driven by a scalar field lying in a false vacuum state. Cosmological inflation provides a mechanism for explaining the specific initial conditions defining the current cosmological model. Inflation produces appropriate density fluctuations for our observable Universe, it explains why the curvature is so close to flat, it provides a scenario for the origin of the matter content within, and explains the properties of the primordial perturbations.

Guth originally came up with the idea of inflation as a solution to the horizon and flatness problems [8]. He described a Universe with an energy density dominated by a single scalar field stuck in a vacuum state at very high temperatures, in an FRW background. As the Universe expanded and the energy scales dropped, another, more stable, vacuum state became accessible. Due to the newly accessible vacuum state, the scalar field continued to evolve according to the Einstein equations in a de Sitter background, causing the Universe to expand at an exponential rate. Eventually, the

phase transition to the stable vacuum started to take place. The Universe was, at that point, a mixture of true and false vacuum regions, with bubbles materialising and expanding at the speed of light, converting nearby regions into the flat and homogeneous FRW Universe. This model had in mind the recent advancements in the symmetry-breaking mechanism and candidates for grand unified theories based on it [9].

The original model predicted that if the bubbles formed too slowly, the phase transition would not occur across the whole Universe. Gott solved the problem by showing that surfaces of constant inflaton encapsulate surfaces with constant negative spatial curvature [10]. In other words, it was shown that the interior of a finite nucleating bubble contains an infinite FRW cosmology, starting from an unstable de Sitter false vacuum configuration. Therefore, there was no need for the entire available volume to percolate, and it was sufficient if a single bubble formed, since it, on its own, could encompass our Universe.

Next, the model of slow-roll inflation was developed as a way to appropriately end inflation [11, 12]. Here, the inflaton also begins in the false vacuum state where it undergoes a first stage of inflation. This period is interrupted when the field crosses the potential barrier, forming a bubble. Inside it, the field continues to roll down the potential hill, from the point where it had exited the barrier, and towards the true minimum. Meanwhile, it goes through a second period of inflation long enough to drive the spatial curvature sufficiently close to zero to match observations. When the field arrives at the bottom of the potential well, it oscillates around the minimum, reheating the Universe, and leading to the conventional hot big-bang cosmology.

The conditions that the slow-roll model placed on the form of the potential and the details of nucleation were used to make predictions about the spectrum of primordial density perturbations that could have been produced in the early Universe [12]. These predictions were compared against modern measurements in order to place constraints on possible inflation models. For example, the quantum fluctuations in the inflaton produce long wavelength scalar curvature and tensor perturbations. These perturbations shape the power spectrum of temperature anisotropies (CMB) on large scales [13].

More complicated models for inflation introduce multiple scalar fields, where each one of these fields fulfils a well-defined role. In the slow roll scenario for example, a large field mass corresponds to more curvature in the false vacuum potential, which leads to more efficient tunneling, but a low mass is important for a successful slow-roll. This balance requirement is lifted if we consider two scalar fields. Having two scalar fields also multiplies the number of observables that can be verified by experiment [13]. At the same time, it comes with the consequence that each inflaton

can decay to a different field value, producing so-called ‘islands’. On these islands, the surfaces of constant field do not coincide, and the resulting Universe is a patchwork of open regions. Again this imposes strict requirements on the model so that it agrees with observations. Increasingly more complicated inflationary models can be formulated, and all rely of Guth’s simple idea of phase transitions.

Another application for phase transitions in the early Universe was described in [14]. The starting point is also a scalar field configuration undergoing false vacuum decay, this time in the context of a first order symmetry-breaking phase transition in physics of (or beyond) the Standard Model, that play a key role in models of baryogenesis. Here, the collision and merging of bubbles produces gravitational waves. The authors in [14] calculated the energy spectrum of the radiated waves in the approximation of linearised gravity. The fraction of vacuum energy liberated in the form of waves was found to be significant, showing that the process could be an important source for the production of a gravitational waves background, analogous to the CMB.

In the modern context, the idea of phase transitions in the early Universe came back along with the rise of string theory [15], and as a way to bring an anthropic resolution to the cosmological constant problem [16]. In these scenarios, inflation is described as a theory of the Multiverse, and the conventional Big Bang is identified as the moment of nucleation of a bubble. These Universes in the form of bubbles are separated by domain walls and materialise from a dense spectrum of vacuum energies. At any time there are regions which are perpetually inflating. The stochastic constants of nature become random through quantum fluctuations of the dynamically evolving inflatons, taking up different values in different parts of the Multiverse.

The most recent motivation for the study of vacuum decay comes from modern particle physics. There is evidence [17] that the Higgs boson is lying in a metastable state and could undergo a phase transition towards a more stable configuration of the Standard Model.

We see that it is therefore worthwhile to study the phenomenon. The standard formalism to study vacuum decay is the instanton-based description developed by Coleman and his collaborators [2, 3]. They developed a quantitative method for computing how fast the process is, and what the bubble looks like, given a potential. In order to come up with the solution, they had reduced the field theoretic problem to an analogy with quantum mechanical tunneling. This description is not time dependent, so details about the correlations between bubbles, or the effect of dynamical fluctuations on the decay rate and the early stages of bubble formation could not be incorporated.

Recently, an alternative formulation was developed, where unlike in the instanton

formalism, quantum fluctuations in the field and its momentum are present around the false vacuum state [1] which accounts for time-evolution. The dynamical tracking is computed using the Wigner formalism. In the present work, we investigate some aspects related to the dynamics of the fluctuations and of vacuum decay. First, we begin to test this novel approach by comparing the properties of a stochastic classical field, generated through computational means, with the analytic properties of a quantum field that has the same power spectrum. We find a very good agreement which proves that the stochastic classical field from our simulations gives rise to a quantum field with the expected statistical properties. Then, we build the formalism to compute bubble-bubble correlations under the assumption that bubbles form at locations of tall peaks in the field. We do so by analytically computing the peak-peak correlation function in a free Gaussian random field, which we were able to match with the statistics of the peaks in the simulated data. We also investigate the effect of fluctuations on the decay rate of two colliding particles lying in the false vacuum state. We argue that this illustrates the correspondence between the inclusion of the fluctuations and first-order quantum corrections. This application can be used to model the probability that collisions of Higgs particles in a high-energy particle accelerator would lead to vacuum decay.

This essay is organised as follows: in Chapter 2, vacuum decay is explained in detail, starting from the work of Coleman, then developing on the semi-classical approach. We describe how this is implemented using a code, which takes stochastically generated field fluctuations as initial conditions, then propagates them according to classical equations of motion. The evolution is determined under the potential derived in [18] for an analogue condensed matter system. The quantum nature of the setup, as well as the time-evolution, is incorporated through the Wigner formalism, and this will be proved in Chapter 3. In Chapter 4 we explain how correlation functions can be obtained from the simulations, and we show that the results are in agreement with quantum field theoretical and statistical predictions. Next, we consider two identical wave-packets of false vacuum field to show qualitatively how classical barrier penetration is amplified by the addition of one-loop order corrections in Chapter 5. We finish by summarising our results and presenting future directions of work in Chapter 6. Appendix A summarises the statistical description of Gaussian random fields, and Appendix B introduces the conventions we used to obtain discrete quantities on a lattice.

2 Vacuum Decay

In a QFT, the vacuum state is defined as the state with the lowest energy, which is annihilated by the annihilation operator, i.e. $\hat{a}|\text{vacuum}\rangle = 0$. To identify this state, we can calculate the effective potential $V(\phi)$ which is the generating functional for 1PI Green's functions with zero external momenta. The ground state of the theory will be the minimum of $V(\phi)$. Consider however a scalar field theory with Lagrangian density

$$\mathcal{L} = \frac{1}{2}\dot{\phi}^2 - \frac{1}{2}(\nabla\phi)^2 - V(\phi), \quad (1)$$

where

$$V(\phi) = V_0 \left(-\cos\phi + \frac{\lambda^2}{2} \sin^2\phi \right). \quad (2)$$

The potential is shown in Fig 1. When $\lambda > 1$, the potential has an infinite periodic sequence of false minima at $\phi = (2n+1)\pi$, alternating with true minima at $\phi = 2n\pi$, where $n \in \mathbb{Z}$. Lambda modulates the depth of the false-vacuum potential wells.

We will assume, for now, that the field ϕ is restricted to only take values in the $[-\frac{\pi}{2}, \frac{3\pi}{2}]$ interval so that we only consider one pair of degenerate minima. In a classical theory, both would be stable and would represent vacuum states. In a quantum theory, barrier penetration renders the state at $\phi_{\text{fv}} = \pi$ unstable.

The standard procedure for calculating quantum tunneling rates is analogous to the Wentzel–Kramers–Brillouin (WKB) approximation for the problem of the single particle trapped in a potential well in non-relativistic quantum mechanics. We describe it in the following section.

2.1 The Instanton Formalism

It is possible to treat the metastable state as the true vacuum state under the assumption that it is sufficiently long-lived, and that the eventual fluctuations have energies much lower than the typical scale of the potential [19]. Then, the field eigenstate at the false vacuum $|\phi_{\text{fv}}\rangle$ can be approximated to the zero eigenstate of the Hamiltonian $H|\phi_n\rangle = E_n|\phi_n\rangle$. Thus, the Euclidean path integral describing the probability of the state remaining in the false vacuum after a time τ can be written as

$$\mathcal{Z} \equiv \langle \phi_{\text{fv}} | e^{-H\tau/\hbar} | \phi_{\text{fv}} \rangle \approx \int_{\phi(0)=\phi_{\text{fv}}}^{\phi(\tau)=\phi_{\text{fv}}} \mathcal{D}\phi e^{-S_E[\phi]}. \quad (3)$$

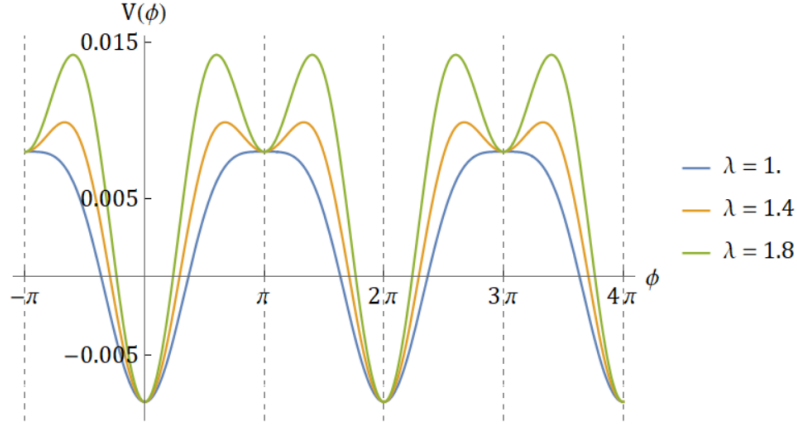


Fig 1. The potential $V(\phi)$ we will use throughout this essay to illustrate vacuum decay. Here, $V_0 = 0.008$. The parameter λ modulates the shape and depth of the sequence of local false minima, which appear for values $\lambda > 1$. These locations for ϕ are unstable against quantum effects.

By inserting a complete set of energy eigenstates into the partition function \mathcal{Z} ,

$$\langle \phi_{\text{fv}} | e^{-H\tau/\hbar} | \phi_{\text{fv}} \rangle = \sum_n e^{E_n\tau/\hbar} \langle \phi_{\text{fv}} | \phi_n \rangle \langle \phi_n | \phi_{\text{fv}} \rangle. \quad (4)$$

The vacuum energy E_0 can be extracted from

$$E_0 = - \lim_{\tau \rightarrow \infty} \frac{\hbar}{\tau} \ln \mathcal{Z}. \quad (5)$$

For an unstable potential, such as the one we are considering, there are no bound states, only resonant states. Resonant states have quantised complex energies, and the decay rate per unit of time is related to the imaginary part of the energy as

$$\Gamma = -2 \text{Im } E_0. \quad (6)$$

To calculate this quantity, we can approximate the path integral by the contribution from its saddle points, known as instanton solutions. The saddle points are trajectories that satisfy the Euclidean equations of motion $\left(\frac{\partial^2}{\partial \tau^2} + \nabla^2 \right) \phi = -V'(\phi)$, and higher order contributions are vanishingly small. The solution to the Euclidean equations of motion with the highest contribution to the path integral has been coined ‘the bounce’, because it starts and ends at the false vacuum. The Euclidean

action of the bounce is given by

$$B \equiv S_E[\phi] = \int dt_E d^d x \left[\frac{1}{2} \left(\frac{\partial \phi}{\partial t_E} \right)^2 + \frac{1}{2} (\nabla \phi)^2 + V(\phi) \right]. \quad (7)$$

S_E is the Euclidean action and $t_E = it$ the imaginary time. The solution with the greatest contribution to B is in general $O(d)$ -symmetric, as was shown in [20] for a single scalar field in d -dimensions. To describe our solution, we may therefore define a new coordinate $\rho^2 = t_E^2 + x^2$ as the Euclidean radius of a $(1+1)$ -dimensional spacetime. The boundary conditions on the field can be summed up as $\lim_{\rho \rightarrow \infty} \phi(\rho) = \phi_{\text{fv}}$, which makes sure that the end state is always the false vacuum. To avoid a singularity, we must also impose $\left. \frac{d\phi}{d\rho} \right|_{\rho=0} = 0$. The equation of motion becomes

$$\frac{d^2 \phi}{d\rho^2} + \frac{d-1}{\rho} \frac{d\phi}{d\rho} = V'(\phi), \quad (8)$$

which for $d = 1+1$ -dimensions corresponds to a particle moving in a one-dimensional potential $-V$, rolling down the hill from the false vacuum towards the true vacuum. There is also a time-dependent damping term, where the time dependency is implied by the variable ρ .

Equation (8) can be integrated numerically. We have used the methods described in [21]. The solution for $\phi(\rho)$ for different choices of λ along with an illustration of the inverted potential are shown in Fig 2. The solution describes the nucleation of a 2-dimensional bubble with radius ρ . Inside the bubble there is the true vacuum, localised at $\phi_{\text{tv}} = 0$, and outside there is the false vacuum, at $\phi_{\text{fv}} = \pi$. The bubble wall is defined as the region where ϕ changes rapidly with increasing ρ . It can be seen from Fig 2b that a larger value of λ corresponds to a smaller difference between energy densities of the relative vacua, and gives rise to a thinner wall. For the smallest value of λ , the wall makes up most of the volume of the bubble.

There are two forces competing on the boundary of the bubble. The true vacuum exerts a pressure on the wall proportional to the volume of the bubble. Another pressure pointing inwards is due to the tension in the wall. Bubbles that form too small collapse, but some by chance are created with a large enough volume to be energetically capable of continuing to expand. A surviving bubble will continue to expand at a speed close to that of light, converting the energy of the false vacuum into the energy needed to continue expanding. The overall energy of such a bubble is zero, so when the bubble does have the right size to expand, it continues to do so until the entire volume lies in the true vacuum.

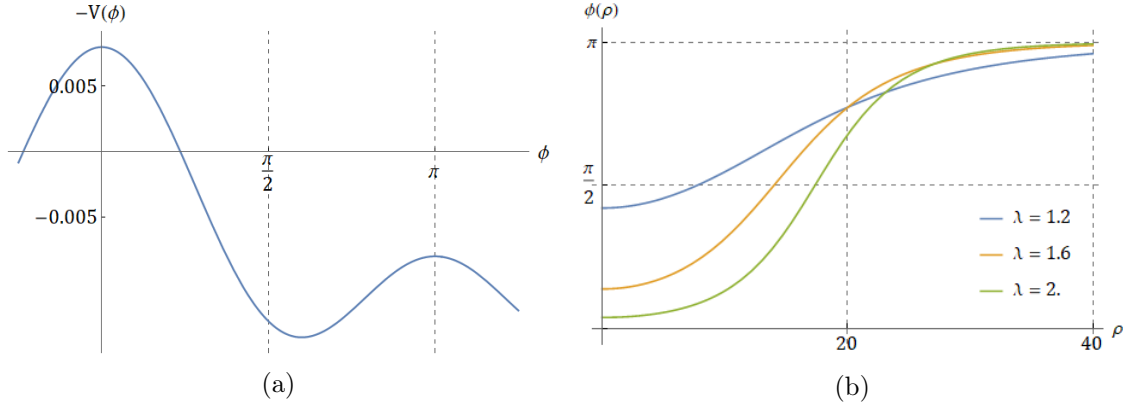


Fig 2. (a) The inverted potential in the equation of motion for the field (8). The solution describes a particle starting at the false vacuum, rolling down the hill towards the true vacuum at $\phi = 0$, moving against a time-dependent drag. (b) The bubble profiles for different values of λ defining the depth of the false vacuum potential well. The bounce solution interpolates between the true and false vacuum solutions to the equation of motion. The bubble wall decreases with increasing λ .

Coleman showed that the decay rate of the false vacuum, or the rate of formation of bubbles, is given by the expression

$$\Gamma \sim A e^{-B/\hbar}, \quad (9)$$

where B is the bounce solution. The proportionality factor A can be calculated by looking at the order \hbar fluctuations around the saddle-point solution. This higher-order contribution is obtained from the Taylor expansion of the action S_E around its maximum. It gives rise to a functional determinant $(\det S''_E[\phi])^{1/2}$ of order 1. Since $V(\phi_{\text{fv}})$ is not a true minimum, the Hamiltonian is unbounded from below, and the field eigenstate at the false vacuum we were mentioning in the first paragraph of this section is not in fact a true energy eigenstate. To proceed, Coleman uses an argument based on the analytic continuation of the action into the complex plane. This causes S''_E to have negative eigenvalues and the determinant becomes imaginary. This explains why it contributes to the decay rate according to equation (6).

We now come back to the periodic potential introduced in (2) and its infinite set of false and true minima. A particle sitting at $\phi_{\text{fv}} = \pi$ would now have several options to tunnel to. This ends up only affecting the overall coefficient to the decay rate, since the Euclidean action is unchanged.

As an aside, we mention that the formalism for incorporating gravitational effects in the context of instantons was developed by Coleman and de Luccia [22]. They

approached this scenario in analogy with the flat instanton case. After computing the classical bounce in Euclidean space, they distorted the path integral over the field into the complex space to run over a saddle point in the action and arrive at the Lorentzian solution, just as before. The inclusion of curvature to the action is done through the addition of a determinant of the metric as a prefactor. When a non-zero value for the potential appears, associated with the apparition of a more stable minimum state, this contributes to the equations of motion under the form of a cosmological constant term, and the underlying spacetime becomes de Sitter. This is the starting point for the theories of the early Universe we have described previously.

To sum up, when the vacuum of a theory corresponds to a non-global minimum, the dominant contribution to the path integral is the solution with the smallest Euclidean action to the classical turning point, and the highest symmetry. This approach allows us to make quantitative predictions about non-perturbative processes such as vacuum decay. Small fluctuations do exist around the solution, but are assumed to be small, contributing only by a prefactor to the overall amplitude of the decay rate. The Euclidean classical field equations yield soliton-like solutions describing bubbles of true vacuum. There exist, in theory, an infinite number of other mechanisms for decay, and it is not known how to assess the accuracy of the saddle-point approximation when it comes to giving the full solution.

2.2 A Semiclassical Approach

A stochastic approach to vacuum decay has been developed as an alternative to the Coleman instanton procedure [1, 23]. In this picture, the field ϕ is initially resting in the false vacuum state, but small fluctuations associated with the quantum zero-point energy are initialised around the state. The fluctuations can be made to undergo dynamical evolution. This is unlike the imaginary time formalism, where time is not properly accounted for. Non-linear evolution leads to the accumulation of large fluctuations in the field. This can be understood by looking at the spectral space decomposition. The Fourier modes in the field reorganise under non-linear evolution such that, by chance, enough energy density can accumulate in a region to propel the field across the potential barrier and to the true vacuum. The probability of the fluctuations being sufficiently large can be computed quantum mechanically using the Wigner formalism, which is described in the next Chapter. This semi-classical approximation remarkably reproduces the right order of magnitude of the exponent in the tunneling rate obtained using the Coleman method [1].

To implement this approach, we use a code to simulate the time evolution of a

1-dimensional field and its conjugate momentum on a discrete lattice. These are initialised according to

$$\phi(x, t = 0) = \phi_{\text{fv}} + \delta\hat{\phi}(x), \quad (10)$$

$$\Pi(x, t = 0) = \delta\hat{\Pi}(x), \quad (11)$$

where ϕ_{fv} is the amplitude of the mean field at the false vacuum. Throughout this work, however, we only consider the field to have non-zero initial value, while the conjugate momentum starts off at zero. Other works investigate the opposite case [24, 25].

In QFT, the ground state is assumed to be Gaussian, such that the spectral modes of the quantum fluctuations are non-interacting. By analogy, the field $\delta\hat{\phi}(x)$ is initialised as a Gaussian random field. In particular, the fluctuations take the form

$$\delta\hat{\phi}(x) = \frac{1}{\sqrt{N}} \sum_k \sqrt{P(k)} \hat{\alpha}_k e^{ik \cdot x}, \quad (12)$$

where the amplitude of each Fourier mode, $\hat{\alpha}_k$, is drawn from a Gaussian distribution and $P(k)$ is the power spectrum of the distribution. The $\hat{\alpha}_k$ are complex Gaussian deviates with unit variance such that $\langle |\alpha_k|^2 \rangle = 1$. These are generated from two independent random variables \hat{a}_k and \hat{b}_k drawn from a uniform distribution on the unit interval that give $\hat{\alpha}_k = \sqrt{-\ln \hat{a}_k} e^{i2\pi \hat{b}_k}$. The values of k in the decomposition of ϕ represent the momentum of each mode in the system.

It is possible to treat equation (12) analogously to the Schrödinger picture relativistic scalar field that has the form [4]

$$\phi(x) = \int \frac{dk}{2\pi} \frac{1}{\sqrt{2\omega_k}} \left(a_k + a_{-k}^\dagger \right) e^{ik \cdot x}, \quad (13)$$

and its conjugate momentum $\Pi(x) = \partial_t \phi(x)$

$$\Pi(x) = \int \frac{dk}{2\pi} (-i) \sqrt{\frac{\omega_k}{2}} \left(a_k - a_{-k}^\dagger \right) e^{ik \cdot x}, \quad (14)$$

by defining their respective power spectra to be

$$\langle \phi_k^* \phi_{k'} \rangle = \frac{1}{2\omega_k} \delta(k - k'), \quad (15)$$

$$\langle \Pi_k^* \Pi_{k'} \rangle = \frac{\omega_k}{2} \delta(k - k'), \quad (16)$$

where $\omega_k^2 = k^2 + m^2$. Here, ϕ_k and Π_k are the spectral modes of the field and its momentum. The mass of the field is proportional to the second derivative in the potential $m^2 = m_{eff}^2 = V''(\phi = \pi) = V_0(\lambda^2 - 1)$. For a Gaussian field, the creation and annihilation operators, a_k and a_k^\dagger respectively, are self-adjoint. Looking back at the discrete version of the fluctuations, we see that the square of the amplitude of the field at each k , $|\phi_k|^2$, is a measure for the occupancy number of each state, since $\hat{N} \equiv \hat{a}_k^\dagger \hat{a}_k$ is the definition of the number operator. Overall, the fluctuations in (10) take the form

$$\delta\hat{\phi}(x) = \frac{1}{\sqrt{2N}} \sum_k^{k_{cut}} e^{ikx} \frac{\hat{a}_k}{(m^2 + k^2)^{1/4}}. \quad (17)$$

This looks like the Fourier transform of a power spectrum $P(k)$ with the expression given by (15), where the amplitude of each mode k is given by the random Gaussian variable \hat{a}_k . The sum is truncated at an arbitrary wavelength k_{cut} . Once again, in our analysis we assume that the initial momentum is null, $\delta\hat{\Pi}(x) = 0$.

The field in the false vacuum, thus initialised, is propagated according to the classical equations of motion, causing the field and momentum modes to evolve and mix. The dynamical evolution for ϕ and Π is obtained by solving

$$\frac{d\phi}{dt} = \frac{\partial \mathcal{H}}{\partial \Pi} = \Pi, \quad \frac{d\Pi}{dt} = -\frac{\partial \mathcal{H}}{\partial \phi} = \nabla^2 \phi - V'(\phi), \quad (18)$$

where \mathcal{H} is the Hamiltonian density. From (1), these are equivalent to

$$\frac{d\phi}{dt} = \Pi, \quad \frac{d\Pi}{dt} = \nabla^2 \phi - V_0 \left(\sin \phi + \frac{\lambda^2}{2} \sin 2\phi \right). \quad (19)$$

It should be noted that the variation of the parameter λ changes the relative importance of the terms in the expression. Having a larger λ leads to having a larger mass, which translates into a higher curvature for the potential wells of false vacuum. In turn, this amplifies the energy conversion from the quadratic to the non-linear terms. Therefore, the evolution leads to a growth of fluctuations, and that eventually causes the false vacuum to decay.

In the next Chapter we explain how the stochastically-generated fluctuations lead to quantum behaviour.

3 The Wigner Formalism

In the instanton method we described in Section 2.1, the dominant contribution to the path integral was obtained by considering classical field expectation values

and assuming that the quantum fluctuations are small and Gaussian. However, when studying phenomena that happen away from equilibrium, such as phase transitions, the fluctuations grow and take over as the dominant contributions to the path integral. This is precisely how vacuum decay can occur in the semi-classical approximation. There are no exact means involving path integrals which can be used to describe the phenomenon. Instead, we may trace the dynamical evolution approximately using a method involving Wigner functionals.

First, we introduce the Wigner function for a particle in $1 + 1$ dimensions with position x and momentum p . This is

$$W(x, p; t) = \frac{1}{\hbar} \int dy e^{-\frac{i}{\hbar} p y} \left\langle x + \frac{y}{2} \left| \hat{\rho}(t) \right| x - \frac{y}{2} \right\rangle, \quad (20)$$

where $\hat{\rho}$ is the density matrix operator in the Schrödinger picture. The Wigner function is a way of representing a quantum state in phase space. It simultaneously contains the information about the probability distributions of both x and p which can be obtained by marginalising over the opposite variable.

The argument below follows [26] and is presented as in the supplemental material to [1]. The Wigner functional can be defined by analogy to the Wigner function as:

$$W[\phi(x), \Pi(x); t] = \int \mathcal{D}\varphi(x) e^{-\frac{i}{\hbar} \int dx \Pi(x) \varphi(x)} \left\langle \phi(x) + \frac{1}{2} \varphi(x) \left| \hat{\rho}(t) \right| \phi(x) - \frac{1}{2} \varphi(x) \right\rangle, \quad (21)$$

where ϕ is the field amplitude and Π its conjugate momentum. From this, expectation values of symmetrised operators $\hat{\mathcal{O}}(\hat{\phi}, \hat{\Pi})$ can be obtained as follows:

$$\langle \hat{\mathcal{O}}(\hat{\phi}, \hat{\Pi}) \rangle \equiv \frac{1}{Z} \int \mathcal{D}\phi(x) \frac{\mathcal{D}\Pi(x)}{2\pi} \mathcal{O}(\phi, \Pi) W[\phi, \Pi; t], \quad (22)$$

$$Z \equiv \text{Tr} \hat{\rho} = \int \mathcal{D}\phi(x) \frac{\mathcal{D}\Pi(x)}{2\pi} W[\phi, \Pi; t]. \quad (23)$$

The left hand side of equation (22) is the average of the physical quantity $\mathcal{O}(\phi, \Pi)$ over the phase space spanned by ϕ and Π , with a distribution function W which characterises the state. Importantly, for the Gaussian state W is always positive definite, and so it can be interpreted as a true probability density function.

If we further consider a most general d -dimensional Hamiltonian of the form:

$$H = \int d^d x \mathcal{H} = \int d^d x \left(\frac{\Pi^2}{2} + \frac{(\nabla \phi)^2}{2} + V(\phi) \right), \quad (24)$$

then the Schrödinger picture density matrix will satisfy the equation of motion:

$$i\hbar \frac{\partial}{\partial t} \hat{\rho}(t) = [\hat{H}, \hat{\rho}(t)]. \quad (25)$$

From here, the equation of motion for the Wigner functional is found to be

$$\left[\frac{\partial}{\partial t} + \int d^d x \left(\Pi \frac{\partial}{\partial \phi} + \nabla^2 \phi \frac{\partial}{\partial \Pi} - \frac{2}{i\hbar} V(\phi) \sin \left(\frac{i\hbar}{2} \overleftarrow{\partial}_\phi \frac{\partial}{\partial \Pi} \right) \right) \right] W[\phi, \Pi; t] = 0, \quad (26)$$

where $\overleftarrow{\partial}_\phi$ acts on the potential to the left. Expanding the last term to second order in \hbar , one obtains the following:

$$\left[\frac{\partial}{\partial t} + \int d^d x \left(\frac{\partial \mathcal{H}}{\partial \Pi} \frac{\partial}{\partial \phi} - \frac{\partial \mathcal{H}}{\partial \phi} \frac{\partial}{\partial \Pi} + \mathcal{O} \left(\hbar^2 V'''(\phi) \frac{\partial^3}{\partial \Pi^3} \right) \right) \right] W[\phi, \Pi; t] = 0. \quad (27)$$

In the semi-classical approach, we may also write the Wigner functional symbolically as $W = W_c + \hbar^2 W_q$, where the letters stand for ‘classical’ and ‘quantum’, respectively. If we also write the previous equation as $(\hat{K}_c + \hbar^2 \hat{K}_q) W = 0$, it follows that, order by order:

$$\hat{K}_c W_c = 0, \quad (28)$$

$$\hat{K}_c W_q + \hat{K}_q W_c = 0. \quad (29)$$

For the periodic potential we are considering, equation (27) shows that our approach is exact, since $V'''(\phi) = 0$ and there are no higher order interactions. When defining the field and its conjugate momentum on the discrete lattice, equation (28) becomes the description of the dynamics of a many-particle system, where the field and its momentum at each lattice point interact with their nearest neighbours via the gradient term in the equations of motion (18). Our code solves equation (28) numerically using a 10th-order in accuracy Gauss-Legendre time integrator [1], and under periodic boundary conditions due to the Fourier discretisation.

It is important to stress once more that we are considering the initial conditions on ϕ and Π to be small fluctuations drawn randomly from a Gaussian distribution centred around the classical expectation value of the false vacuum. Thus, each field value can be represented in the Wigner functional as a finite sum over discrete points in phase space. From the argument of the previous paragraph, this captures the time evolution of the expectation values of the field and momentum on the lattice, to one-loop order. The field and conjugate momentum propagate classically, but encompass the quantum evolution of the system. The state of the field can be recovered at

late times by measuring the Wigner functional and computing ensemble averages of many different realisations with different random initial conditions.

Over the following two Chapters, we will consider two applications that allow us to go beyond the instanton formalism and explore the dynamics of the quantum fluctuations in the relativistic setting. We will look at correlation functions in the free Gaussian random field, as a precursor to computing bubble correlations. Then, we will look at the contribution of the fluctuations on vacuum decay induced by the scattering of scalar particles.

4 Towards the Bubble-Bubble Correlation Function

In this Chapter we explore the statistics of the free Gaussian random field. Our goal is to build the formalism required to compute the correlation between the bubble nucleation sites in the field at the false vacuum. The Gaussian random field approximation is accurate for deep false vacuum wells, i.e. for high λ .

In a relativistic first order phase transition, the usual assumption is that bubbles form at random throughout the space, and that there is no preference for one space-time point or another, meaning that there is no seeding. However, from Gaussian peak theory, as we will see, the tallest peaks manifest clustering. Our hypothesis is that the bubbles form around these tallest peaks in the field, and we want to test whether the bubbles themselves cluster.

This investigation is motivated by cosmology. Primordial density perturbations in the early Universe are also thought to be Gaussian. These perturbations grow until they reach a critical density, becoming insensitive to the expansion of the Universe. Instead, they collapse into dark matter halos, where matter accumulates to form large structures, such as galaxies. The statistical properties of the peaks are, in this context too, a measure of clustering and non-linearity. The formalism developed in this Chapter builds the tools necessary to test our hypothesis and measure the statistics of the field around bubble nucleation sites.

Starting from the existence of zero-point fluctuations, we replace the potential in equation (2) by the mass term

$$V(\phi(x)) = \frac{m^2}{2}\phi(x)^2 \quad (30)$$

in the equations of motion. Here, our field is exactly Gaussian and the evolution of the Wigner functional in equation (27) is also exact, i.e. $V \sim \phi^2$. We initialise the field and the momentum around the classical solutions $\phi_{\text{cl}} = 0$, as opposed to

$\phi_{\text{fv}} = \pi$, and $\Pi(0, x)_{\text{cl}} = \Pi(0, x)_{\text{fv}} = 0$. Therefore, the only non-zero quantity at $t = 0$ is the field of fluctuations, $\delta\phi(x)$ which has the form described in Chapter A.

We first compute the relativistic two-point correlation functions for this field. We do this in order to validate our approach: first we check the statistical properties of the simulated field, and then that we are able to measure the state of the field at any time. In the second part of this Chapter we then shift our analysis to measuring the clustering of peaks in the free field.

4.1 The Two-Point Autocorrelation Function

We begin by computing the two-point field-field correlation function which we denote $\langle\phi(x)\phi(y)\rangle$, where x and y are spacetime coordinates. From the QFT perspective, this object represents the amplitude for a particle to propagate from spacetime coordinate $y = (y^0, y^1)$ to coordinate $x = (x^0, x^1)$. We also introduce $k = (\omega_k, k^1)$. In the Heisenberg picture, for the relativistic scalar field in $1+1$ dimensions, the correlation function is

$$\langle\phi(x)\phi(y)\rangle = \int \frac{dk}{2\pi} \frac{1}{2\omega_k} e^{-ik \cdot (x-y)} = \int \frac{dk}{2\pi} \frac{1}{2\omega_k} e^{+i\omega_k(x^0-y^0)-ik^1(x^1-k^1)}, \quad (31)$$

which is a Lorentz invariant quantity. Then, for a spacelike interval $x - y$, we can always perform a change of coordinates such that $|x^1 - y^1| = r, r > 0$ and $x^0 - y^0 = 0$ such that

$$\langle\phi(x^0 = 0, x^1)\phi(y^0 = 0, y^1)\rangle = \int_{-\infty}^{\infty} \frac{dk}{2\pi} \frac{e^{-ik^1 r}}{2\sqrt{k^{12} + m^2}} = \frac{1}{2\pi} K_0(m|r|), \quad (32)$$

where $K_0(x)$ is a modified Bessel function of the second kind. On the other hand, if the interval is taken to be timelike, i.e. $|x^1 - y^1| = 0$ and $x^0 - y^0 = t, t > 0$, then:

$$\langle\phi(x^0, 0)\phi(y^0, 0)\rangle = \int_{-\infty}^{\infty} \frac{dk}{2\pi} \frac{e^{i\omega_k t}}{2\omega_k} = \int_m^{\infty} \frac{d\omega_k}{2\pi} \frac{e^{i\omega_k t}}{2\sqrt{\omega_k^2 - m^2}} \stackrel{t \rightarrow \infty}{=} \frac{1}{4\pi} K_0(-imt). \quad (33)$$

For the free scalar field, the quantities above are exact. It is only if we add interactions that we would need to consider higher order corrections in order to fully describe the theory.

Considering that we are working on a discrete lattice, the expressions above change according to the conventions outlined in Appendix B. The two-point correlation functions for the free scalar field have the discrete form

$$\langle\phi(0, x^1)\phi(0, y^1)\rangle = \sum_{k=1}^{k_n} P(k) e^{-i2\pi k(x-y)/N}, \quad (34)$$

where k_n is an arbitrary cutoff and

$$\langle \phi(x^0, 0) \phi(y^0, 0) \rangle = \sum_{k=1}^{k_n} P(k) e^{-i\omega_k t dt}. \quad (35)$$

$P(k)$ is the discrete power spectrum with the form

$$P(k) \sim (k^2 dk^2 + m^2)^{-1/2}, \quad (36)$$

and we have omitted the normalisation factor. A similar set of expressions can be obtained for $\Pi = \partial_t \phi$. Here in the discrete version, x , t and k are natural numbers indexing the lattice sites up to N .

To compute these quantities from the simulated data, we start by initialising a field from stochastic fluctuations around the power spectrum (36), and allow it to evolve as described in Section 2.2. We introduce the maximal cut-off scale for the sampling of the Fourier amplitudes at $k_{\text{Nyquist}} = N/2 + 1$, where N is the number of lattice sites, here chosen as $N = 1024$. We produced a total of 3000 simulations, each with a different realisation of initial amplitudes for the spectral space field modes. In order to test the Lorentz symmetry of the relativistic field, we sampled the field amplitude at random points on the lattice, in both coordinates. This arbitrary field value was multiplied by another amplitude at a distance r away, for the spacelike correlator, or at a time t away for the timelike correlator. Importantly, because of the periodicity in the x coordinate, the sampling of the separation r ends at $N/2$ where N is the number of lattice sites. The expectation value was obtained by averaging across all simulations.

The correlation function obtained from the data was compared against the expression in equations (34) and (35). The result is shown in Fig 3 for both the true and the smoothed field. For the smoothing we use a Gaussian filter over a scale σ to effectively dampen the high frequency modes. Note how the smoothing has the effect of introducing an apparent non-locality: the spacelike two-point correlation function falls off less abruptly with increasing filtering scale σ . Details about the effect of the filter and the implementation of the lattice discretisation can be found in Appendix B.

Thus, we have proved that the code we are using accurately computes the time evolution of a field with the right power spectrum and statistical properties of a relativistic scalar massive quantum field. We now move on to computing the peak-peak correlation function for the same free Gaussian random field.

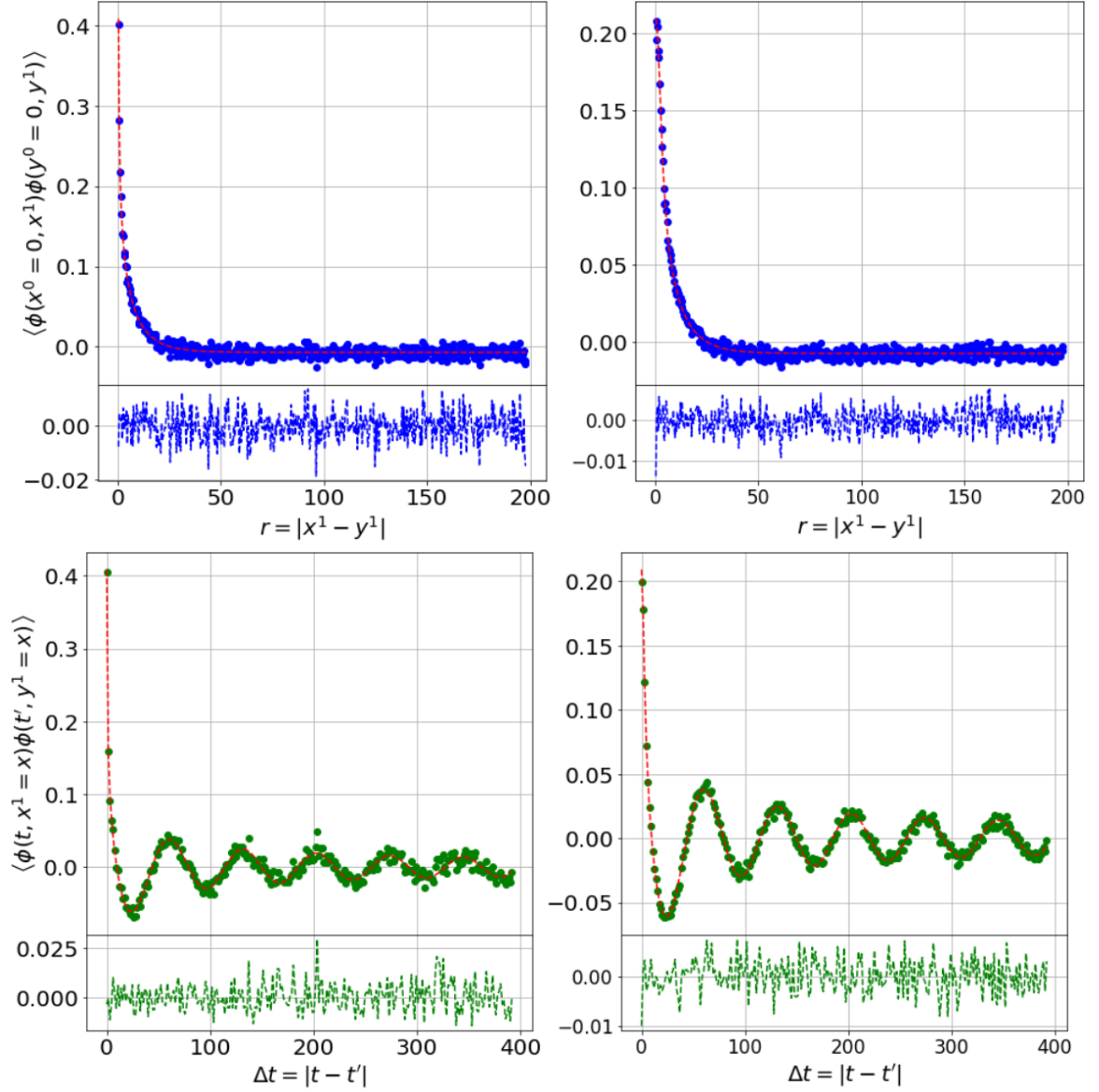


Fig 3. The spacelike and timelike-separated correlation functions for the free relativistic scalar field. The dotted red curve is the QFT prediction for a field with mass m . The data points are ensemble averages of the product of field amplitudes at a separation r on the circular lattice of size $L \sim 400$. The field is initialised with random amplitudes for each spectral mode, drawn from a Gaussian distribution with unit standard deviation. The bottom panel in each picture shows the numerical error of the data against the prediction. It decreases as $1/\sqrt{S}$, where S is the total number of field realisations in the ensemble. The left hand side images show the same correlator, for a field smoothed on a scale $\sim m^{-1}$. The oscillatory behaviour in the timelike correlator functions is related to the fact that the Gaussian field rearranges itself over time scales $\sim m^{-1}$.

4.2 The Peak-Peak Correlation Function

Another important statistical quantity is the peak-peak correlation function. We will only consider the smoothed field in this Chapter, such that everywhere we let $\phi(x, \sigma) \equiv \phi(x)$, where σ is once again the full width at half maximum of the smoothing Gaussian window.

The properties of peaks in an underlying Gaussian random field can be analysed using a rigorous formalism, which predicts the number density of peaks as a function of peak height, and the peak-peak correlation function. The following derivations follow the steps described in [5]. Here, the distribution of peaks in the Gaussian random field is described as a Poisson point process, i.e. their number density is a sum of Dirac delta functions:

$$n_{pk}(x) = \sum_{pk} \delta(x - x_{pk}), \quad (37)$$

where x_{pk} are the locations of peaks. Expanding the field $\phi(x)$ and its gradient $\eta(x) \equiv \nabla\phi(x)$ around the field maximum we obtain that

$$\phi(x) \approx \phi(x_{pk}) + \frac{1}{2}\zeta(x - x_{pk})^2, \quad (38)$$

$$\eta(x) \approx \zeta(x - x_{pk}), \quad (39)$$

where $\zeta(x) = \nabla^2\phi(x)$.

We can impose further constraints on the variables to obtain the peaks by imposing certain physical criteria on the field maxima. For example, in the equations above we have used that at a maximum, the first derivative must be null. At the same time, we must enforce that the second derivative $\zeta(x)$ is strictly negative at x_{pk} such that we are extracting only a maximum of the field, and not a minimum. The last constraint we want to enforce is on the height of the peak, which should be above some imposed threshold.

It follows that $x - x_{pk} \approx \zeta^{-1}(x_{pk})\eta(x)$, and so $\delta(x - x_{pk}) = |\zeta(x_{pk})|\delta(\eta(x))$. The Dirac deltas will then pick up the points that are zeros of $\eta(x)$. The number density of extrema of ϕ becomes

$$n_{ext}(x) = \zeta(x)\delta(\eta(x)), \quad (40)$$

since we have not yet imposed explicitly that ζ should be negative. The ensemble average of this equation is given by:

$$\langle n_{pk}(x) \rangle \equiv \langle \zeta(x)\delta(\eta(x)) \rangle = \int \mathcal{P}(\phi, \eta = 0, \zeta < 0) \zeta \, d\zeta \, d\phi, \quad (41)$$

where $\mathcal{P}(\phi, \eta, \zeta) d\phi d\eta d\zeta$ is the Gaussian probability distribution for the field, where the vector of variables \vec{y} is taken as $(\phi, \nabla\phi, \nabla^2\phi)$. This follows the notation in equation (60) in Appendix A.

One can then compute the covariance matrix with elements $\mathcal{M}_{ij} = \langle y_i y_j \rangle$ using the definition as:

$$\sigma_{(m+n)/2}^2 = \left\langle y_i^{(m)}(x) y_j^{(n)}(x) \right\rangle = \int_{-\infty}^{\infty} dk k^{m+n} P(k; \sigma), \quad (42)$$

where $y^{(m)} = \frac{d^m y}{dx^m}$ and $\sigma_{(m+n)/2}$ are the moments of the distribution. Discretising and substituting for the scalar power spectrum this gives:

$$\sigma_{(m+n)/2}^2 = \frac{1}{N} \sum_{k_j=1}^{k_{nyq}} (dk k_j)^{m+n} \frac{e^{-(dk k_j \sigma)^2}}{\sqrt{(dk k_j)^2 + m^2}}, \quad (43)$$

which is a discrete quantity that can be computed from simulation data. The symmetric covariance matrix then has non-zero elements $\mathcal{M}_{11} = \sigma_0^2$, $\mathcal{M}_{22} = \sigma_1^2$, $\mathcal{M}_{33} = \sigma_2^2$, and $\mathcal{M}_{13} = -\sigma_1^2$.

The physical constraints we placed on the parameters ϕ, η and ζ motivate the introduction of some characteristic scales for the parameters. The peak height is conventionally expressed in terms of the zeroth moment, $\sigma_0^2 = \langle \phi(x) \phi(x) \rangle^{1/2}$, which represents the mean of the field. We will also express ζ in terms of its second moment, $\sigma_2^2 = \langle \nabla^2 \phi(x) \nabla^2 \phi(x) \rangle^{1/2}$, since the Laplacian is naturally a convenient measure of steepness. The following notation will be used:

$$\nu \equiv \frac{\phi}{\sigma_0}, \quad q \equiv \frac{\zeta}{\sigma_2}. \quad (44)$$

The equation (41) obeying all of the physical constraints for selecting the peaks, becomes under this notation:

$$n_{\text{pk}}(\nu_t) = - \int_{\nu_t \sigma_0}^{\infty} \int_{-\infty}^0 \mathcal{P}(\phi, \eta = 0, \zeta; \mathcal{M}) \zeta d\zeta d\phi \quad (45)$$

$$= \frac{-\sigma_0 \sigma_2^2}{\sqrt{(2\pi)^3 \det \mathcal{M}}} \int_{\nu_t}^{\infty} \int_{-\infty}^0 q e^{-\frac{1}{2} \vec{y} \cdot \mathcal{M}^{-1} \cdot \vec{y}} dq d\nu. \quad (46)$$

Both integrals can be solved analytically in Mathematica [27], for the appropriate choice of parameters. The result depends on the number of lattice sites and the smoothing function. We have worked with a smoothing scale $\sigma = 0.02/m$ where m is

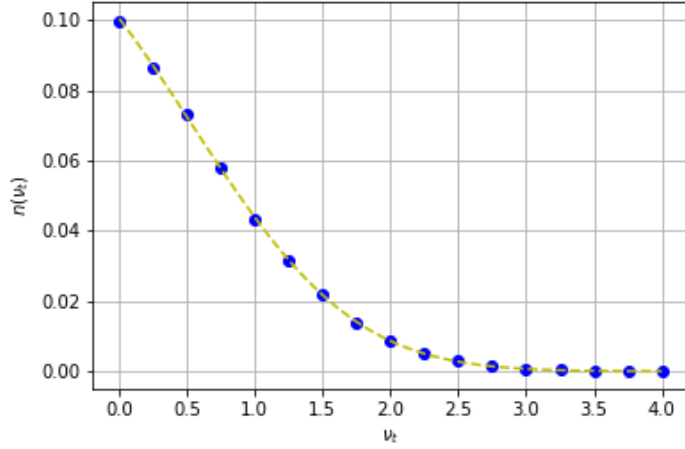


Fig 4. The peak number density for a Gaussian random field, plotted against a detection threshold, multiple of the standard deviation in the field amplitude. The yellow curve is the analytical prediction. The number of peaks falls linearly with increasing peak height, and virtually no peaks exist beyond three standard deviations in the peak amplitude. This observation is valid for all the lattice sizes we have inspected.

the field mass, since for $\sigma \sim m$ the field is distorted, but in the absence of a filtering scale, the lattice separation can shield the possibility of apparition and measurement of strongly clustered peaks, i.e. we would miss peaks at separations < 1 unit of lattice separation.

We have also computed the peak number density as a function of detection threshold from data. To do so, we took another 3000 simulations, for a lattice of size $N = 4096$. From each simulation we have chosen at random a single timeslice, then we obtained the number of peaks within, and divided by the size of the lattice. The ensemble average was computed, giving the analogous quantity from data to the function we have just derived analytically above. The results agree well with each other as can be seen in Fig 4.

Now we turn to the derivation of the peak-peak correlation function. First, the n -point correlation function of peaks is defined in terms of the peak number density as:

$$1 + \xi_{\text{pk}}^{(n)}(x_1, \dots, x_n) = \langle n_{\text{pk}}(x_1) \cdots n_{\text{pk}}(x_n) \rangle / \langle n_{\text{pk}} \rangle^n, \quad (47)$$

which is the joint probability that a peak exists in every volume element dx_i . The variables describing each peak ϕ, η and ζ are defined at each point so that $\vec{y}_{(n)} = (\phi_1, \eta_1, \zeta_1, \dots, \phi_n, \eta_n, \zeta_n)$.

We are interested in the two-point correlation function. In terms of the Gaussian

probability distribution, and assuming that both peaks are detected above the same threshold height, this is

$$1 + \xi_{pk}(r) = \frac{1}{n_{pk}(\nu_t)^2} \iint_{\nu_t \sigma_0}^{\infty} \iint_{-\infty}^0 \mathcal{P}(\phi_1, 0, \zeta_1, \phi_2, 0, \zeta_2) \zeta_1 \zeta_2 d\zeta_1 d\zeta_2 d\phi_1 d\phi_2, \quad (48)$$

where r is the separation between the two peaks.

Now the covariance matrix has dimensions 6×6 and the entries are dependent on the peak separation. The spectral moments at separate spatial points have an extra factor to account for the separation

$$\xi_{(m+n)/2}(r) = \left\langle y_i^{(m)}(x) y_j^{(n)}(x + x_{ij}) \right\rangle \quad (49)$$

$$= \int_{-\infty}^{\infty} dk k^{m+n} P(k) \begin{cases} \cos(k x_{ij}), & m+n \text{ even} \\ \sin(k x_{ij}), & m+n \text{ odd} \end{cases} \quad (50)$$

where $P(k)$ is the same field power spectrum and

$$x_{ij} = \begin{cases} 0, & i = j \\ r, & i \neq j. \end{cases} \quad (51)$$

The new covariance matrix has non-zero elements $\mathcal{M}_{14} = \xi_0(r)$, $\mathcal{M}_{24} = -\mathcal{M}_{15} = \xi_{1/2}(r)$, $\mathcal{M}_{16} = -\mathcal{M}_{25} = \mathcal{M}_{34} = -\xi_1(r)$, $\mathcal{M}_{35} = -\mathcal{M}_{26} = \xi_{3/2}(r)$, and $\mathcal{M}_{36} = \xi_2(r)$. The submatrices \mathcal{M}_{ij} , $i, j = 1, 2, 3$, and \mathcal{M}_{kl} with $k, l = 4, 5, 6$, are defined from two-point correlation functions at the same spatial points respectively. Therefore they both equal the previous matrix. The symmetry property $\mathcal{M}_{ij} = \mathcal{M}_{ji}$ is true for all indices.

The full expression for the peak-peak correlation function takes the following form:

$$1 + \xi_{pk}(r) = \frac{\sigma_0^2 \sigma_2^4}{n_{pk}^2(\nu_t) \sqrt{(2\pi)^6 \det \mathcal{M}}} \iint_{\nu_t}^{\infty} \iint_0^{\infty} q_1 q_2 e^{-\frac{1}{2} \vec{y} \cdot \mathcal{M}^{-1} \cdot \vec{y}} dq_1 dq_2 d\nu_1 d\nu_2, \quad (52)$$

where $\vec{y} = (\phi_1, \eta_1 = 0, \zeta_1, \phi_2, \eta_2 = 0, \zeta_2)$. This expression is computed exactly using methods available in Mathematica for integration of multiple integrals.

Once again we may discretise the autocorrelation functions $\xi_{(m+n)/2}(x)$, in order to find the equivalent expression that can be compared against the data from our simulations. In order to obtain the correlation function on the lattice, we chose two algorithms similar to those used by the first galaxy surveys [28, 29].

To extract the peak-peak correlation function from data, we consider again the Poisson point process. The connected two-point correlation function ξ_{pk} is the excess probability, i.e. relative to a Poisson distribution, of finding a field maximum in both volumes dx and $d(x+r)$, a distance r apart:

$$d\mathcal{P} = n_{pk}^2 (1 + \xi_{pk}(r)) dx d(x+r), \quad (53)$$

where n_{pk} is the number density of peaks on the lattice. With this interpretation in mind, we can extract the correlation function from the data using the following estimator by [29]

$$1 + \xi_{pk}(r) = \frac{GG(r)}{RR(r)}, \quad (54)$$

where $GG(r)\Delta r$ is the number of pairs of peaks with separation in the range r to $r \pm \Delta r/2$. $RR(r)\Delta r$ is the expected number of such pairs, had the peaks been sampled from a uniform distribution. Any deviation of the estimator from 0 indicates spatial clustering. The periodic boundary conditions of the lattice are useful in that we may forget about finite size effects around the edges. In terms of the effective data sampling, we chose $\Delta r = 2$ lattice sites. Note that the field is effectively lying on a circle, so the separation between any two peaks was taken to be the smallest distance between them.

The second estimator by [28] has the following form:

$$1 + \xi_{pk}(r) = \sum_i \frac{G_i}{n_{pk}\Delta r}, \quad (55)$$

where G_i is the number of peaks in the neighbourhood of volume Δr of peak i , n_{pk} is the number density of peaks on the timeslice, and we sum over all the peaks on the timeslice. Then we obtain the ensemble average over the simulations. We have checked that two estimators agree identically with each other, in the limit of large $RR(r)$.

We have checked that the data agrees with the theoretical result for three different detection thresholds: $\nu_t = 1, 1.5$, and 2 . In all cases we obtained a good fit, and the results are shown in Fig 5 for estimator (55). The results shown here correspond to $N = 8192$, $\sigma = 0.005/m$, and $S = 500$. For larger values of threshold, $\nu_t \geq 2$, we found that there were insufficient peaks under this criterion to be able to obtain accurate results. We checked however that for large lattices, $N \sim 2^{15}$, data also matches the expected result for $\nu_t > 2$. However, making many instances of such simulations to obtain precise averages is very demanding computationally (one such simulation compiles in over 5h per timeslice). We therefore conclude that the

prediction is good, so long as there are sufficient peaks satisfying the selection criteria (> 50) per timeslice, such that making statistical calculations is possible.

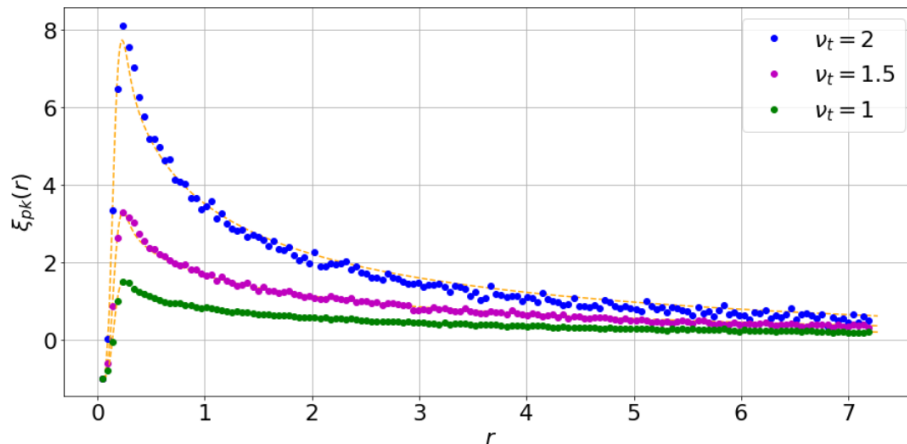


Fig 5. The peak-peak correlation function for three detection thresholds. The peaks cluster on scales where the correlation function ξ_{pk} is positive. This is most significant at low separation. The exponential fall around $r \rightarrow 0$ indicates the scale of the smoothing function which uniformises the field. The function continues to fall off at larger scales reaching progressively more negative values, noting that r is bound by $L/2 \sim 200$. Larger detection thresholds correspond to a larger peak in ξ_{pk} and thus more clustering on those scales.

In the next section, we will look at a direct application of vacuum decay, and show how the existence of the fluctuations gives rise to corrections to a classical result.

5 Vacuum Decay from Scattering

We have shown in Chapter 3 that the Wigner framework allows us to obtain one-loop order corrections to the classical trajectory. In this Chapter we illustrate the power of this formalism by looking at a familiar case of dynamical evolution in quantum field theory: the collision of two false vacuum particles. We return to the potential introduced in equation (2). The effect of the periodicity in the potential is that we have to bear in mind that the field can decay to either side of its false vacuum well. Two illustrative events are shown in Fig 6. For performing this experiment, we chose a value of λ for which the decay rate is effectively zero for the duration of the collision. We will see how despite this, the addition of fluctuations changes significantly the overall decay rate for a large region in the parameter space of the collision energy.

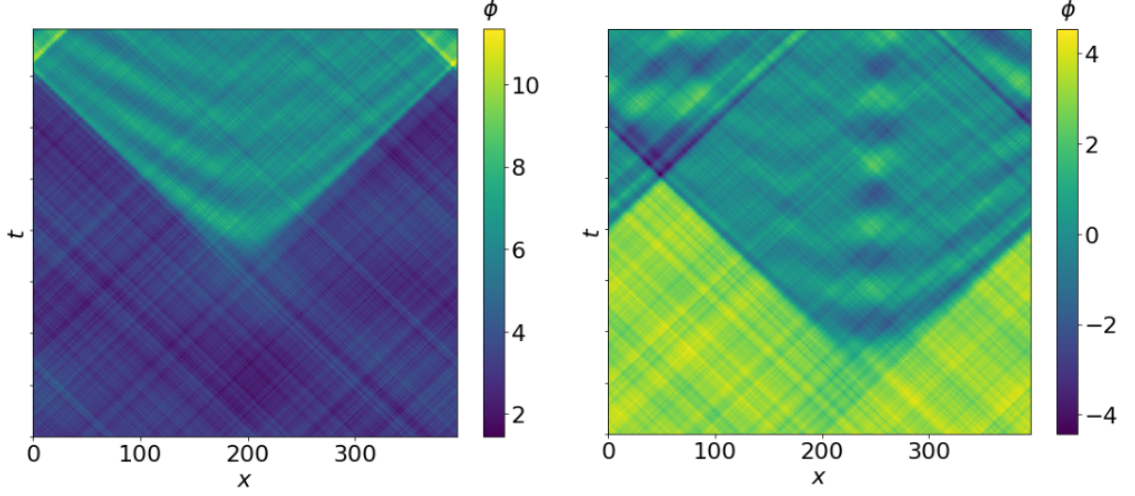


Fig 6. The spacetime diagrams of two nucleation events for $\lambda = 1.2$. The field at time $t = 0$ is initialised around the false vacuum state at $\phi_{\text{fv}} = \pi$. Propagation according to potential (2) leads to non-linear evolution for the modes that eventually causes the field to decay to the true vacuum state. There are two options, one at $\phi_{\text{tv}} = 0$ shown on the right, and another at $\phi_{\text{tv}} = 2\pi$ in the left image. The value of the field across the diagram is shown in the colour bar. The wave-like features appearing inside the bubbles last while the field is seeking to reach equilibrium in the new state. The features are the most evident where the opposite boundaries of the bubble collide due to the periodic boundary conditions. The bubble starts off its expansion in a fuzzy region, quickly reaching the speed of light to produce a lightcone.

The wave-packets are modelled in the code as two identical Gaussian shells, directed towards each other. This is achieved by initialising the field as

$$\phi(0, x) = A e^{-\frac{(x-x_w)^2}{2\varepsilon^2}}, \quad (56)$$

$$\Pi(0, x) = -\frac{\delta\alpha}{\varepsilon} (x - x_w) A e^{-\frac{(x-x_w)^2}{2\varepsilon^2}} \sim \partial_x \phi(0, x), \quad (57)$$

where A and ε are the amplitude and width of the wave-packet, which is localised at x_w . $\delta = \pm 1$ determines the direction of propagation, while α is an arbitrary damping factor for the momentum. The observation that $\Pi(t=0, x) \sim \partial_x \phi$ instead of $\sim \partial_t \phi$ is a manifestation of the $O(2)$ symmetry in the classical solution at initialisation. In terms of the fluctuations, $\delta\phi(t=0, x)$ and $\delta\Pi(t=0, x)$, these have the same form as described in Chapter 2.2. However, the spectral cutoff is set to $k_{\text{cut}} = N/4$.

As the wave-packets collide, they interact strongly via the gradient term in the equations of motion of the field. From a classical point of view, the field decays once

the energy density in some region of the space overcomes the energy density of the potential barrier. The non-linear evolution of the equations of motion converts some of the kinetic energy of the field into gradient energy which may eventually suffice to form a nucleation site.

By taking the Fourier transform of the Coleman prediction for the bubble profile solution with this choice of λ , it is possible to obtain the range of Fourier momenta which are the most important during the formation of a bubble. We found that the event corresponds to a steep increase in the amplitudes of the lowest modes on the lattice. Therefore, we expect the longest wavelength frequencies to be the most efficient in causing decay.

The equations of motion and the shape of the wave-packet imply that a certain amount of the energy will disperse during propagation. The energy dispersed will travel at the speed of light. In a scattering experiment, particles collide and then scatter off towards infinity, where they are detected. Here, the periodic boundary conditions mean that we must choose a lattice with a size N much greater than the initial distance between the wave-packets, in order to avoid the dispersed energy to re-enter the system. The event is considered to last between the moment when the means of the wave-packets intersect, and until the null surfaces of the wave-packets intersect a second time i.e. before the dispersed energy returns into the system. This is roughly the same amount of time it takes for the means of the wave packets to cross half of the lattice.

For this experiment, we considered two values for the initial wave-packet momentum, one corresponding to $\alpha = 0.5$, and the second to $\alpha = 1$. The parameter space was spanned by A and ε . Both parameters start off close to zero. The amplitude A was capped above $\pi/2$, while the width ε was considered far into a regime where the wave-packets have overlapping regions, where $\varepsilon \sim L/6$, and L is the physical size of the lattice. We have thus maximised the available space of collision energies.

The same parameter space was covered three times: first, by only one wave-packet; second, by two wave-packets, and third by 2 wave-packets with fluctuations. We looked at the decay of only one wave-packet to leave out of our statistics the decay events which were not due to a collision event, but rather because the energy of a single wavepacket was enough for it to cross the barrier on its own.

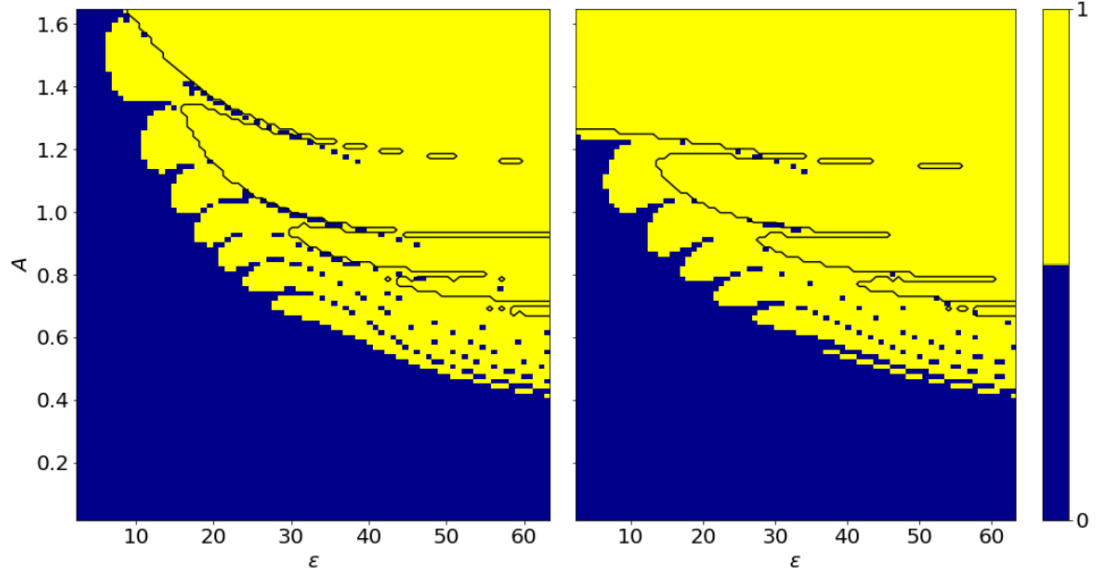
It should be noted that we have checked explicitly that the decay rate was not influenced by the size of the lattice. This was done by investigating the time it took for one wave-packet to decay, varying only the number of modes available on the lattice, i.e. the number of lattice sites. We found no change.

The outcome for the collision of two wave-packets is showed in Figure 7a. The contoured region separates the sampling space between the region where decay hap-

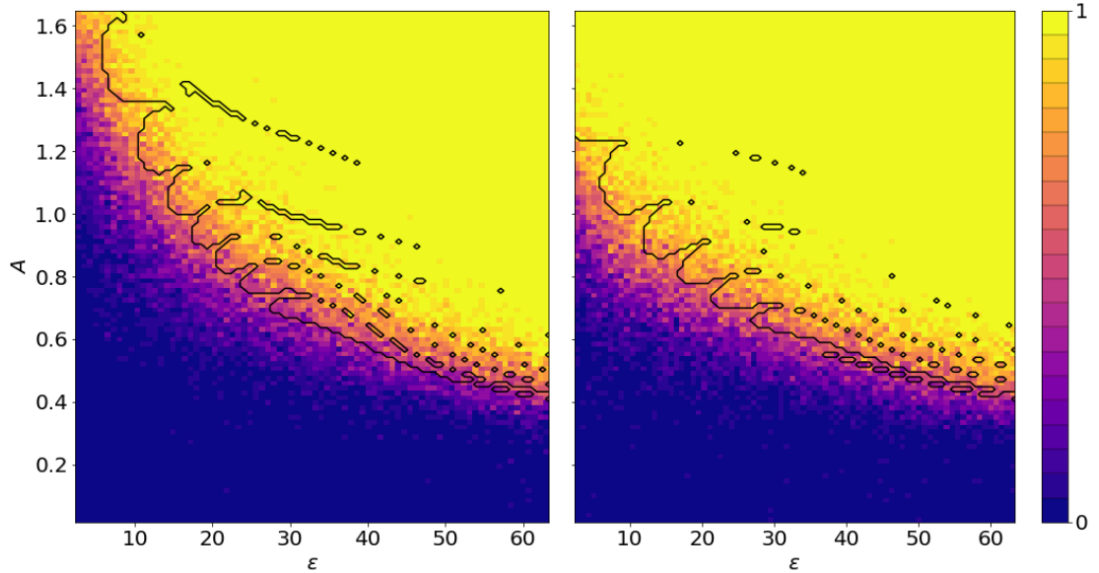
pens due to the collision event, and where it happens for a single wave-packet, where the latter appears at higher energies. It can be seen that the figure of the right hand side, corresponding to a higher momentum, covers a greater region in the width axis, but the decay stops at exactly the same value in amplitude. Therefore, there seems to exist an amplitude below which decay is classically forbidden. However, it looks like a more efficient momentum conversion from the field to its conjugate momentum can induce decay in the highly localised particles. The resonance bands hint at a cancelling of low frequency modes, which obstructs the decay. In the classical case, the decay rate is binary: either there is enough energy to overcome the potential barrier, or there isn't.

Even when the collision of two wave-packets did not induce decay, it still contributed with significant amounts of energy to the target volume. Once we added the quantum fluctuations, we obtained a positive decay rate for a much larger region in the parameter space. The results are shown in Fig 7b. The 'decay balance' is as follows. Each image is made of 8400 pixels. For the $\alpha = 0.5$ case, there are 1300 decay events due to the collision, and a total of 2999 pixels with a non-zero decay rate, when we add fluctuations. We have subtracted from both totals the 3013 pixels which represent the decay of a single wave-packet. Overall, the collision induced a total of 4131 certain events, while adding the fluctuations lowered that to 3311. For the $\alpha = 1$ case, a single wave-packet decays 3625 times. There are an additional 1254 pixels in the classical collision case, but 2797 additional pixels with fluctuations. The total number of events due to the collision is 4879, and the total number of events that happened with probability 1 in the case with fluctuations is 3979. A total number of 352800 simulations was required to produce Figures 7a and 7b.

Therefore, there is no doubt that the inclusion of vacuum fluctuations amplifies the overall decay rate. It should be noted that the occurrence of the decay is affected both negatively and positively by the fluctuations. These can either contribute to, or have a dissipative effect on the process of bubble formation, from the energy of the collision. By comparing with the instanton solution, this seems to be due to the shorter-wavelength modes in the fluctuations. This experiment shows that we can think of the bubbles as macroscopic objects, forming due to the apparition of quantum fluctuations. From this point of view, the classical properties of the system are acquired through a process of decoherence, where high-energy modes take the role of the 'environment'.



(a) The contour separates the regions where decay happens for a single wave-packet, and where it is due to the collision itself. The colour bar shows the decay rate.



(b) The decay rate is computed out of a total of 20 simulations for each sampled point. The contour shows the edge of the classically allowed domain in Fig 7a above.

Fig 7. We show the range of scattering-induced vacuum decay by sampling values in the amplitude and the width of identical particles modelled as Gaussian wave-packets. The results are shown for two values of initial momentum, where the images on the left correspond to $\alpha = 0.5$, and the ones on the right to $\alpha = 1$. The top figures show the classically allowed region, while the bottom ones show the effect of additional quantum zero-point fluctuations. These increase the space of values that can induce a phase transition by 51% when $\alpha = 0.5$, and 32% for $\alpha = 1$. The number of certain events changes by -23% and -18% , respectively.

6 Conclusion

We have showed that it is possible to obtain vacuum decay from a real-time formalism, by introducing stochastic fluctuations around the vacuum state of a real scalar field. We computed the correlation functions for the free field in order to gain insight into the statistical properties of our theory. We have also arrived at the correlation function between peaks in a Gaussian random field. The next step in this direction is to repeat the analysis for the field lying in the false vacuum state. There, we can gain some insight into the correlations between the bubbles that form around the true vacuum state, by zooming into the field region around the nucleation sites and checking how the statistics compare to the Gaussian case. Another straightforward extension would be to compute the mean bubble profile from the simulations. This can be compared against the Coleman prediction. When the quantum noise is averaged out, the comparison should shed more light on whether the two mechanisms describe the same decay channel, i.e. if the spherical instanton approximation is well-justified.

We have also calculated from simulations the effect of fluctuations on the collision-induced decay rate, and we found a clear amplification. The same analysis can be specialised and applied to the problem of approximating the probability of decay for the Higgs field in high-energy collisions, for an appropriate choice of parameters and the relevant shape of the potential.

One problem we have not investigated is the evolution of the field inside the bubble, where there are fewer inhomogeneities and the field is self-correlated on larger scales. Moreover, we do not have a description for the dynamics of the field at the bubble wall, particularly in the thick-wall case. In fact, in all the literature that the author is aware of, many approximation schemes are used to describe the wall, and very strong constraints are in place.

With respect to this point, a particularly interesting prospect for understanding the phenomenon comes from the possibility of performing an analogue experiment. Recent papers have described how to simulate false vacuum decay in flat space using a cold matter system [30, 31]. Such an experiment can be used to test without any approximations the physics of the phenomenon.

Broadly, the possible generalisations of the picture outlined here are many. For example, an important generalisation would be the introduction of thermal fluctuations besides the stochastic ones. Another generalisation should take into account gravitational effects. These would open many interesting research paths that would shed more light on cosmological applications, as described in Chapter 1, from the dynamics of inflationary models, to collisions of bubbles regarded as entire Universes.

7 Acknowledgements

First of all, I am thankful to my supervisor, Matt Johnson, for his mentorship and guidance, at every step throughout the project and in the process of writing this essay. He has motivated me to work with joy and curiosity, and always helped me to move forward. I am eagerly anticipating our continuing collaboration.

I am also indebted to Iván Burbano for helping me ensure the mathematical rigour of both computational and analytical parts of my work, as well as for his helpful suggestions with respect to this essay. More than that, I am grateful that he took upon himself the challenge to always remind me that happiness and good health go hand in hand with a solid work ethic. I dedicate my essay to him.

Lastly, I want to mention my parents. Despite being far away, they have remained my constant and unconditional support and backbone throughout my academic pursuit.

References

- [1] J. Braden, M. C. Johnson, H. V. Peiris, A. Pontzen, and S. Weinfurtner, “New Semiclassical Picture of Vacuum Decay,” *Physical Review Letters* **123** no. 3, (Jul, 2019) 031601.
- [2] S. Coleman, “Fate of the false vacuum: Semiclassical theory,” *Physical Review D* **15** no. 10, (May, 1977) 2929–2936.
- [3] C. G. Callan and S. Coleman, “Fate of the false vacuum. II. First quantum corrections,” *Physical Review D* **16** no. 6, (Sep, 1977) 1762–1768.
- [4] D. Peskin, Michael; Schroeder, *An Introduction to Quantum Field Theory*. Perseus Books Publishing L.L.C., 1995.
- [5] J. M. Bardeen, J. R. Bond, N. Kaiser, and A. S. Szalay, “The statistics of peaks of Gaussian random fields,” *The Astrophysical Journal* **304** (May, 1986) 15.
- [6] S. L. Lumsden, A. F. Heavens, and J. A. Peacock, “The clustering of peaks in a random Gaussian field,” *Monthly Notices of the Royal Astronomical Society* **238** no. 2, (May, 1989) 293–318.
- [7] J. Braden, “1d-scalar.” <https://github.com/jonathanbraden/1d-Scalar>, 2019.

-
- [8] A. H. Guth, “Inflationary universe: A possible solution to the horizon and flatness problems,” *Physical Review D* **23** no. 2, (Jan, 1981) 347–356.
 - [9] A. H. Guth and E. J. Weinberg, “Cosmological consequences of a first-order phase transition in the SU(5) grand unified model,” *Physical Review D* **23** no. 4, (Feb, 1981) 876–885.
 - [10] J. R. Gott, “Creation of open universes from de Sitter space,” *Nature* **295** no. 5847, (Jan, 1982) 304–307.
 - [11] A. D. Linde, “A new inflationary universe scenario: A possible solution of the horizon, flatness, homogeneity, isotropy and primordial monopole problems,” *Physics Letters B* **108** no. 6, (1982) 389–393.
 - [12] M. Bucher, A. S. Goldhaber, and N. Turok, “Open universe from inflation,” *Physical Review D* **52** no. 6, (Sep, 1995) 3314–3337.
 - [13] J. Garcia-Bellido, “Single-bubble Open Inflation: An Overview,” tech. rep., 2nd International Workshop on Birth of the Univers, Rome, Italy, Mar, 1997.
 - [14] A. Kosowsky and M. S. Turner, “Gravitational radiation from colliding vacuum bubbles: Envelope approximation to many-bubble collisions,” *Physical Review D* **47** no. 10, (May, 1993) 4372–4391.
 - [15] S. Kachru, R. Kallosh, A. Linde, and S. P. Trivedi, “de Sitter vacua in string theory,” *Physical Review D* **68** no. 4, (Aug, 2003) 046005.
 - [16] A. Vilenkin, *Anthropic predictions: the case of the cosmological constant*, p. 163–180. Cambridge University Press, 2007.
 - [17] J. Ellis, J. R. Espinosa, G. F. Giudice, A. Hoecker, and A. Riotto, “The probable fate of the Standard Model,” *Physics Letters, Section B: Nuclear, Elementary Particle and High-Energy Physics* **679** no. 4, (2009) 369–375.
 - [18] J. Braden, M. C. Johnson, H. V. Peiris, A. Pontzen, and S. Weinfurtner, “Nonlinear dynamics of the cold atom analog false vacuum,” *Journal of High Energy Physics* **2019** no. 10, (Oct, 2019) 174.
 - [19] M. P. Hertzberg and M. Yamada, “Vacuum decay in real time and imaginary time formalisms,” *Physical Review D* **100** no. 1, (Jul, 2019) 016011.

- [20] S. Coleman, V. Glaser, and A. Martin, “Action minima among solutions to a class of Euclidean scalar field equations,” *Communications in Mathematical Physics* **58** no. 2, (1978) 211–221.
- [21] A. Masoumi, K. D. Olum, and B. Shlaer, “Efficient numerical solution to vacuum decay with many fields,” *Journal of Cosmology and Astroparticle Physics* **2017** no. 01, (Jan, 2017) 051–051.
- [22] S. Coleman and F. De Luccia, “Gravitational effects on and of vacuum decay,” *Physical Review D* **21** no. 12, (Jun, 1980) 3305–3315.
- [23] A. Linde, “Stochastic approach to tunneling and baby universe formation,” *Nuclear Physics B* **372** no. 1-2, (Mar, 1992) 421–442.
- [24] S.-J. Wang, “Occurrence of semiclassical vacuum decay,” *Physical Review D* **100** no. 9, (Nov, 2019) 096019.
- [25] J. J. Blanco-Pillado, H. Deng, and A. Vilenkin, “Flyover vacuum decay,” *Journal of Cosmology and Astroparticle Physics* **2019** no. 12, (Dec, 2019) 001–001.
- [26] S. Mrówczyński and B. Müller, “Wigner functional approach to quantum field dynamics,” *Physical Review D* **50** no. 12, (Dec, 1994) 7542–7552.
- [27] W. R. Inc., “Mathematica, Version 12.1.”. Champaign, IL, 2020.
- [28] A. R. Rivolo, “The two-point galaxy correlation function of the Local Supercluster,” *The Astrophysical Journal* **301** (Feb, 1986) 70.
- [29] M. Davis, A. Meiksin, M. A. Strauss, L. N. da Costa, and A. Yahil, “On the universality of the two-point galaxy correlation function,” *The Astrophysical Journal* **333** (Oct, 1988) L9.
- [30] O. Fialko, B. Opanchuk, A. I. Sidorov, P. D. Drummond, and J. Brand, “The universe on a table top: engineering quantum decay of a relativistic scalar field from a metastable vacuum,” *Journal of Physics B: Atomic, Molecular and Optical Physics* **50** no. 2, (Jan, 2017) 024003.
- [31] J. Braden, M. C. Johnson, H. V. Peiris, and S. Weinfurtner, “Towards the cold atom analog false vacuum,” *Journal of High Energy Physics* **2018** no. 7, (Jul, 2018) 14.

A Statistics of the Free Gaussian Random Field

The statistical properties of the density perturbations are described by the probability distribution function of the field:

$$\mathcal{P}_x(\phi_1, \phi_2, \dots, \phi_n) d\phi_1 d\phi_2 \dots d\phi_n, \quad (58)$$

which gives the probability that the density field $\phi(x)$ has values between ϕ_i and $\phi_i + d\phi_i$ at position $x_i, i = 1, 2, \dots, n$. The distribution is fully determined by its moments:

$$\langle \phi_1^{l_1} \phi_2^{l_2} \dots \phi_n^{l_n} \rangle \equiv \int \phi_1^{l_1} \phi_2^{l_2} \dots \phi_n^{l_n} \mathcal{P}_x(\phi_1, \phi_2, \dots, \phi_n) d\phi_1 d\phi_2 \dots d\phi_n, \quad (59)$$

where $l_i \in \mathbb{N}$. If the field is sampled from a Gaussian distribution, then the probability distribution for random variables y_i is

$$\mathcal{P}(y_1 y_2 \dots y_n) dy_1 dy_2 \dots dy_n = \frac{e^{-\mathcal{O}}}{\sqrt{(2\pi)^n \det(\mathcal{M})}} dy_1 dy_2 \dots dy_n, \quad (60)$$

$$\mathcal{O} = \frac{1}{2} \sum_{i,j} \Delta y_i (\mathcal{M}^{-1})_{ij} \Delta y_j, \quad (61)$$

where $\mathcal{M}_{ij} \equiv \langle \Delta y_i \Delta y_j \rangle$ is the covariance matrix and Δy_i are fluctuations about their mean. The multivariate Gaussian distribution functions have the same statistical properties as the field, i.e. isotropy and homogeneity. This means that the moments are translationally and rotationally invariant.

The density field can also be described by its Fourier transform. The statistical properties of the spectral modes come from the distribution function:

$$\mathcal{P}_k(\phi_{k_1}, \phi_{k_2}, \dots, \phi_{k_n}) d|\phi_{k_1}| d|\phi_{k_2}| \dots d|\phi_{k_n}|, \quad (62)$$

which gives the probability that the modes ϕ_{k_i} have amplitudes in the range $|\phi_{k_i}|$ and $|\phi_{k_i}| + d|\phi_{k_i}|$. Similarly to \mathcal{P}_x , \mathcal{P}_k is fully determined if all of its moments are known. Importantly, the second moment, $P(k) = \langle \phi_k \phi_{-k} \rangle$, is the power spectrum of the density field.

Therefore, we can relate the two-point autocorrelation function of the field and the power spectrum by a Fourier transform:

$$\xi(x - y) = \langle \phi(x) \phi(y) \rangle = \int_{-\infty}^{+\infty} \frac{dk}{2\pi} P(k) e^{ik \cdot (x - y)}. \quad (63)$$

Any linear combination of Gaussian variates is itself a Gaussian, and so is its Fourier transform. A consequence of this is that we may consider only the upper-half space of spectral modes to specify the field, as $\phi_k^* = \phi_{-k}$. This motivates the conventions in Appendix B. It can also be shown that all Fourier modes are mutually independent, propagating individually on the circular lattice. Another consequence is that no correlation functions of higher order than $\xi(r)$ can be non-zero. Therefore, $\xi(x, y)$ completely specifies the statistical properties of the density field.

By applying a Gaussian filter to the density field on the scale σ leads to the new field

$$\phi(x; \sigma) = \int \frac{dx'}{\sqrt{2\pi}\sigma} \phi(x') e^{-\frac{1}{2}\left(\frac{x-x'}{\sigma}\right)^2}. \quad (64)$$

By the convolution theorem, the Fourier components and power spectrum change as well on the same scale given by σ

$$\phi(k; \sigma) = \phi_k e^{-\frac{1}{2}(k\sigma)^2}, \quad (65)$$

$$P(k; \sigma) = P(k) e^{-(k\sigma)^2}. \quad (66)$$

In order to accurately determine the values these expressions take on a lattice, it is necessary to first determine the discrete version.

B Lattice Field Theory

On a discrete lattice we can define the following maps:

$$f : \{1, \dots, N\} \rightarrow \mathbb{R}, \quad \mathcal{F}(f) : \{1, \dots, N\} \rightarrow \mathbb{R}. \quad (67)$$

Then, the working Fourier transform convention on the lattice of size N is the following:

$$\mathcal{F}(f)(j) = \sum_{i=1}^N e^{i\frac{2\pi}{N}i \cdot j} f(i), \quad \mathcal{F}^{-1}(\tilde{f})(i) = \sum_{j=1}^N e^{-i\frac{2\pi}{N}i \cdot j} \tilde{f}(j) \quad (68)$$

In terms of the scalar field in the simulation, we can represent it in the same way:

$$\tilde{\phi}(k) = \sum_x e^{-ikx} \phi(x), \quad \phi(x) = \frac{1}{N} \sum_k e^{ikx} \tilde{\phi}(k). \quad (69)$$

The Kronecker delta on the lattice takes the following form:

$$\frac{1}{N} \sum_{i=1}^N e^{-i\frac{2\pi}{N}i \cdot (j-k)} = \delta_{j,k}. \quad (70)$$

This is a very useful result for converting quantities from the continuous to the discrete regimes.

Applying a Gaussian filter on the field is equivalent to multiplying each Fourier mode of the field by a Gaussian centred at the origin, and periodic with period N which we write as $G_i(j) = \frac{1}{\sqrt{2\pi}\sigma} e^{-\frac{1}{2}\left(\frac{j-i}{\sigma}\right)^2}$. The convolution in real space for the field ϕ at site i and its Fourier transform into spectral space look like

$$\phi_{\text{sm}}(i) = \sum_{j=1}^N \phi(j) G_i(j), \quad (71)$$

$$\mathcal{F}(\phi_{\text{sm}}(i)) = \mathcal{F}(\phi(i)) \mathcal{F}(G_0(i)). \quad (72)$$

The Gaussian filter must be normalised to unity in real space such that it does not distort the field. Then, the filter effectively dampens the frequencies near $k = N/2$, but leaves lowest and highest frequencies untouched. However, it does not make sense to consider frequencies above k_{nyq} , the Nyquist frequency, and so both the spectral space filter $\mathcal{F}(G(x)) \equiv G(k) = e^{-\frac{1}{2}(k\sigma)^2}$ and the spectral field $\tilde{\phi}(k)$ are truncated there.

The quantities x and k are indexed by natural numbers on the lattice, such that the analysis must take units into account when working with physical quantities. Specifically, $x = \frac{L}{N}x_i \equiv dx x_i$, and $k = \frac{2\pi}{N}k_j \equiv dk k_j$, where $x_i, k_j \in \mathbb{N}$, L is the physical size of the lattice, and N the number of lattice sites. The integrals over momentum and position are turned into sums over the respective indices.

The spatial Laplacian in the equations of motion is computed by differentiating the field so defined with the spatial index as argument. Therefore, both the real and spectral space lattices have periodic boundary conditions with period N .

Lastly, as mentioned, we are considering experimental parameters motivated by applications in condensed matter systems. Their values are fixed throughout our study and specifically they are: the physical size $L = 25/\sqrt{\mu}$, $V_0 = 4\mu$, $m = \sqrt{4\mu(\lambda^2 - 1)}$, $\lambda = 1.5$ and $\mu = 2 * 10^{-3}$, where μ is the transition rate between two Bose-Einstein condensate species. All details are shown in [18].

The physical volume L is divided into an arbitrary number of lattice sites, depending on the requirements of the problem. For example, in order to have significant clustering in the peak correlation function, we needed to consider a very dense lattice with $N = 8192$, such that a great number of modes can coexist. In the scattering experiment, the vast number of simulations that were required to map the entire parameter space meant that we had to compromise on the size of the lattice, and we chose $N = 256$.